

# FuXi-Nowcast: Meet the longstanding challenge of convective initiation in nowcasting

Lei Chen<sup>1†</sup>, Zijian Zhu<sup>1†</sup>, Xiaoran Zhuang<sup>2,3†</sup>, Tianyuan Qi<sup>1</sup>,  
Yuxuan Feng<sup>2,3</sup>, Xiaohui Zhong<sup>1\*</sup>, Hao Li<sup>1\*</sup>

<sup>1</sup>Artificial Intelligence Innovation and Incubation Institute, Fudan University, Shanghai, 200433, China.

<sup>2</sup>Jiangsu Meteorological Observatory, Nanjing, Jiangsu, 210008, China.

<sup>3</sup>Jiangsu Key Laboratory of Severe Storm Disaster Risk / Key Laboratory of Transportation Meteorology of CMA, Nanjing, Jiangsu, 210008, China.

\*Corresponding author(s). E-mail(s): [x7zhong@gmail.com](mailto:x7zhong@gmail.com);  
[lihao\\_lh@fudan.edu.cn](mailto:lihao_lh@fudan.edu.cn);

Contributing authors: [cltpys@163.com](mailto:cltpys@163.com); [24210240443@m.fudan.edu.cn](mailto:24210240443@m.fudan.edu.cn);  
[zxrxz3212009@163.com](mailto:zxrxz3212009@163.com); [25213050312@m.fudan.edu.cn](mailto:25213050312@m.fudan.edu.cn);  
[fengyuxuan27@163.com](mailto:fengyuxuan27@163.com);

†These authors contributed equally to this work.

## Abstract

Accurate nowcasting of convective storms remains a major challenge for operational forecasting, particularly for convective initiation and the evolution of high-impact rainfall and strong winds. Here we present FuXi-Nowcast, a deep-learning system that jointly predicts composite radar reflectivity, surface precipitation, near-surface temperature, wind speed and wind gusts at 1-km resolution over eastern China. FuXi-Nowcast integrates multi-source observations, such as radar, surface stations and the High-Resolution Land Data Assimilation System (HRLDAS), with three-dimensional atmospheric fields from the machine-learning weather model FuXi-2.0 within a multi-task Swin-Transformer architecture. A convective signal enhancement module and distribution-aware hybrid loss functions are designed to preserve intense convective structures and mitigate the rapid intensity decay common in deep-learning nowcasts. FuXi-Nowcast surpasses the operational CMA-MESO 3-km numerical model in Critical Success Index for reflectivity, precipitation and wind gusts across thresholds and

lead times up to 12 h, with the largest gains for heavy rainfall. Case studies further show that FuXi-Nowcast more accurately captures the timing, location and structure of convective initiation and subsequent evolution of convection. These results demonstrate that coupling three-dimensional machine-learning forecasts with high-resolution observations can provide multi-hazard, long-lead nowcasts that outperforms current operational systems.

**Keywords:** nowcasting, convective initiation, FuXi-Nowcast, radar, extreme

## 1 Introduction

The intensifying impacts of climate change are driving more frequent and destructive high-impact weather events, such as strong winds and heavy rainfall, with growing threats to socio-economic stability and public safety [1–5]. Therefore, accurate high-resolution weather forecasts are essential for effective climate adaptation and disaster mitigation. Nowcasting, the very short-term weather prediction over the next 0–6 hours, plays an increasingly important role [6–8]. It relies on real-time, high-resolution observations to describe the current atmospheric state and predict its immediate evolution [2]. The urgent need for accurate nowcasting arises from the inherent limitations of conventional physics-based numerical weather prediction (NWP) systems at short lead times. Due to computational latency, infrequent updates, and model spin-up issues [9–11], NWP forecasts show reduced forecast skill during the first few hours, particularly for localized, high-impact weather events [12–14].

Despite their importance, existing nowcasting methods face several persistent limitations. First, they often fail to predict convective initiation (CI), the onset of the first convective cells, which provides crucial early warnings for thunderstorms. CI is typically defined as the first occurrence of radar reflectivity exceeding 35–40 dBZ [15, 16], and remains a long-standing challenge due to the complex cloud characteristics and pre-convection environments. Classical approaches, such as the Thunderstorm Identification, Tracking, Analysis and Nowcasting algorithm (TITAN), typically only identify and track echoes once they reach 30–35 dBZ [17], while optical flow-based approaches [18] extrapolate radar echo displacement but can not effectively predict convection initiation, intensification, or decay [19–22]. These deficiencies stem from their reliance on radar reflectivity alone [20], which lacks three-dimensional atmospheric information about the pre-convective environment [9, 19]. Even when augmented with satellite data, computational costs constrain their skill in predicting convective evolution [11]. Machine learning nowcasting models, such as PredRNN [23] and DGMR [10], show similar issues, often producing unrealistic rapid decay of strong convection. Second, extrapolation-based methods lose forecast skill rapidly beyond about 2 hours [19], as localized radar data alone is insufficient to represent the large-scale atmospheric drivers of weather evolution [21]. Although recent machine learning models have extended the skillful precipitation nowcasting using assimilated NWP analyses, their dependence on NWP analyses introduces latency and error propagation [24, 25]. Third, most existing methods remain limited to a single-variable or single-modality forecasting.

Traditional techniques that combine radar and ground-based observations often forecast only precipitation [26], while advanced machine learning models such as MetNet [27] and MetNet-2 [24] also primarily focus on rainfall. Yet operational applications require simultaneous monitoring and forecasting of multiple hazards, such as heavy rainfall and strong wind gusts, making single-variable models inadequate [10, 28, 29].

Recent developments have sought to overcome these limitations. Embedding physical constraints into machine learning models has improved predictions of convective initiation and evolution. For instance, NowcastNet [28] combines a stochastic generative network with a deterministic evolution network to capture multiscale atmospheric dynamics, producing physically plausible, high-resolution precipitation fields. nowcasts with sharp multiscale patterns. The MetNet series integrates assimilated NWP fields to extend skillful lead times from 8 to 24 hours [24, 25, 27], and MetNet-3 further achieves multi-variable prediction of precipitation, wind, temperature, and dew point [25]. Recent efforts also exploit multi-source data such as ground-based and Global Navigation Satellite System (GNSS) observations for multi-hazard nowcasting [8, 30].

Despite these advances, several key challenges remain. Most long-lead machine learning nowcasting models remain constrained by their dependence on NWP analyses, which suffer from latency of 6-8 hours in some leading global NWP models, such as the high-resolution forecasts (HRES) of the European Centre for Medium-Range Weather Forecasts (ECMWF) [31]. Moreover, no existing model simultaneously achieves long skillful lead times, multi-variable prediction, and accurate representation of strong convection. Therefore, developing an multi-variable nowcasting models that is independent of NWP and capable of capturing CI and maintaining the strength of predicted strong convection, remain a significant challenge.

Here, we introduce FuXi-Nowcast, a machine learning nowcasting model capable of simultaneously processing and forecasting multiple meteorological variables, including 2-meter temperature (T2M), wind gusts (GS), wind speed (WS), composite reflectivity (CR), and total precipitation (TP). Using a multi-task learning framework with customized weighted loss functions, FuXi-Nowcast effectively fuse multi-source inputs, such as station observations, radar reflectivity, the High-Resolution CMA Land Data Assimilation System (HRCLDAS) [32, 33], and a machine learning-based weather prediction model forecasts (in this paper FuXi [34]), while preserving fine-scale details and handling skewed distributions. To improve CI prediction, FuXi-Nowcast integrates three-dimensional atmospheric forecasts from FuXi-2.0 [34, 35], a state-of-the-art machine learning-based weather forecasting model. This design enables long lead-time forecasting without relying on traditional NWP systems, mitigating their computational cost and update latency while maintaining the sensitivity to large-scale circulation. To further alleviate the common problem of intensity decay in machine learning-based nowcasting, FuXi-Nowcast employs a feature enhancement module that dynamically amplifies the key convective signals during end-to-end training, preserving intensity and spatial coherence and mitigating premature dissipation of strong convection. Results demonstrate that FuXi-Nowcast outperforms both traditional NWP models. It provides accurate multi-variable forecasts and delivers higher skill within the critical 0–6 hour nowcasting window, effectively capturing the full life cycle of convective systems from initiation to dissipation.

## 2 Results

We evaluate the 12-hour forecast performance of FuXi-Nowcast and CMA-MESO for TP, CR, and GS, using data from April to July 2024. Quantitative evaluation is based on the Critical Success Index (CSI), complemented by case studies assessing each model's ability to predict convective initiation.

All forecasts are initialized every 3 hours with a 1-hour temporal resolution. CR and GS are evaluated against observations, while TP is evaluated using the HRCLDAS dataset as reference.

### 2.1 Overall statistical performance

Figure 1 compares the CSI performance of FuXi-Nowcast and CMA-MESO for CR, TP, and GS at three intensity thresholds. The y-axes vary among thresholds for each variable. As expected, the forecast skill for both models declines with increasing lead time and intensity threshold.

FuXi-Nowcast consistently outperforms the CMA-MESO model across all variables. For CR, FuXi-Nowcast achieves higher CSI scores almost throughout the 12-hour forecast period, with its advantage becoming more pronounced after the first few hours. The most pronounced improvement is observed for TP. Although CSI values for heavy rainfall ( $TP > 20$  and  $40$  mm) remain low for both models, reflecting the intrinsic forecast challenge, FuXi-Nowcast maintains a distinct advantage, while CMA-MESO's CSI scores decline to near zero. For GS, FuXi-Nowcast also shows superior and stable across all thresholds, except at lead times beyond 6 hours when the GS threshold is 17.2 m/s. Overall, FuXi-Nowcast provides a robust and consistent performance advantage, particularly for high-impact events such as heavy rainfall, underscoring its potential for operational nowcasting.

### Model Performance Comparison: Critical Success Index (CSI)

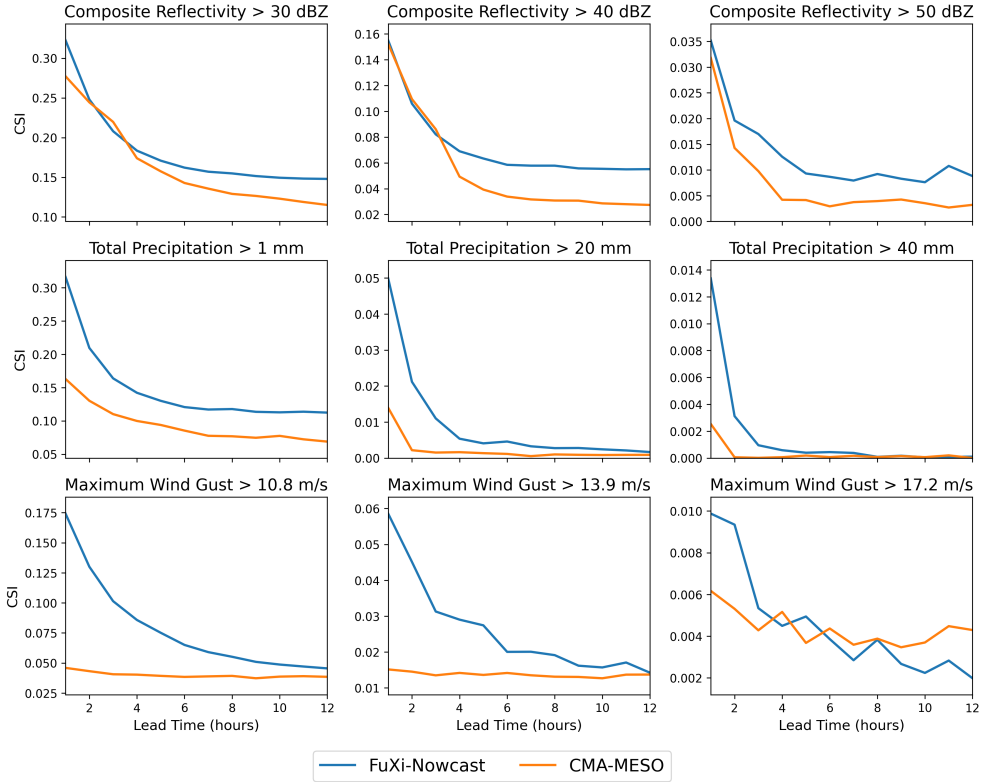


**Fig. 1** Comparison of the Critical Success Index (CSI) for FuXi-Nowcast (blue line) and CMA-MESO (orange line) in 12-hour forecasts. Rows 1 to 3 correspond to composite reflectivity (CR), total precipitation (TP), and wind gust (WS), respectively. Columns represent three increasing intensity thresholds for each variable (from left to right). Higher CSI values indicate better forecast performance.

## 2.2 Convective event forecasting

A severe convective event occurred at 9 UTC on 16 June 2025, triggered by a dry-line and resulting in convective precipitation. As shown in Figure 2, comparison with observed CR from 10 to 14 UTC illustrates that FuXi-Nowcast more accurately reproduced quasi-linear convection that developed over central Jiangsu around 12 UTC, both in terms of location and intensity. FuXi-Nowcast captures the timing of convective initiation, showing no significant echoes at a 1-hour lead time and convective cells exceeding 30 dBZ first appearing at T + 3 h (12 UTC). Although the predicted intensity is slightly weaker than observed, the spatial structure closely matches the radar observations.

In contrast, CMA-MESO produces convective cores exceeding 35 dBZ as early as  $T + 1$  h. However, its temporal evolution diverges from observations, with reflectivity peaking prematurely at  $T + 3$  h and dissipating rapidly thereafter. Consequently, CMA-MESO largely fails to predict the observed precipitation around 12 UTC, resulting in an almost complete miss. Overall, FuXi-Nowcast demonstrates superior capability in capturing the timing of convective initiation and reproducing the structural evolution of convective systems compared with CMA-MESO.

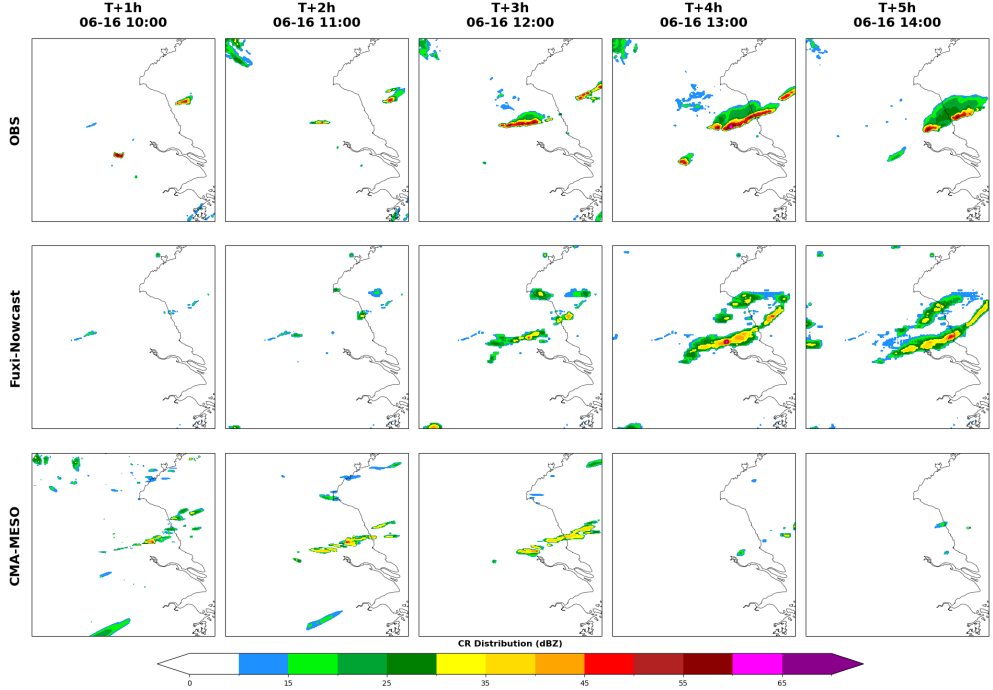


**Fig. 2** Composite radar reflectivity (dBZ) over East China ( $29.01^{\circ}\text{N}$  -  $36.68^{\circ}\text{N}$ ,  $114.67^{\circ}\text{E}$  -  $123.62^{\circ}\text{E}$ ) for a case initialized at 09 UTC 16 June 2025. Rows from top to bottom show observations, FuXi-Nowcast forecasts, and CMA-MESO forecasts, respectively. Columns from left to right correspond to forecast lead time of 1 to 5 hours, valid from 10 to 14 UTC. The color bar denotes reflectivity values from 0 to 65 dBZ.

### 3 Discussion

Convective forecasting, particularly convective initiation, and its subsequent evolution, has long posed a major challenge in nowcasting. Conventional approaches such as extrapolation-based methods, struggle to predict convective initiation, while deep learning models often suffer from rapid intensity decay when forecasting severe convection. Here, we present FuXi-Nowcast, a deep learning-based nowcasting framework designed to overcome these limitations by improving the prediction of convective

initiation and evolution, extending skillful forecast lead times, and enabling multi-variable forecasting. FuXi-Nowcast successfully resolve convective initiation processes that conventional methods fail to capture and substantially alleviates the intensity decay commonly observed in deep learning models. It also outperforms the operational NWP model, CMA-MESO, across multiple statistical metrics and thresholds.

FuXi-Nowcast integrates large-scale three-dimensional atmospheric fields from a machine learning-based weather forecasting model, and learns the moisture and dynamic conditions that potentially trigger convection, information that local observations alone cannot adequately provide. A feature enhancement module identifies and tracks convective cells to better maintain extreme convective intensities, alleviating the intensity decay. In addition, a multi-task learning framework with customized weighted loss functions enables simultaneous and effective multi-hazard forecasting.

Despite these advances, several limitations remain. First, the model's capability to precisely localize convective initiation requires further improvement. Incorporating additional high-resolution data sources, such as satellite data, is expected to improve forecasting performance. Second, case studies reveal that CMA-MESO occasionally outperforms FuXi model in capturing certain small-scale features. This suggests a promising avenue for future development: employing regional models to generate high-resolution three-dimensional atmospheric data "ground truth" to train models that downscale and correct global model outputs, thereby providing FuXi-Nowcast with improved three-dimensional physical inputs. Finally, further validation across diverse regions is needed to assess the model's generalization capability.

In conclusion, FuXi-Nowcast represents a significant step toward next-generation nowcasting systems. By improving the prediction of convective initiation and evolution, mitigating intensity decay in extreme events, and enabling multi-hazard forecasting, FuXi-Nowcast advances the frontier of data-driven nowcasting. The integration of large-scale three-dimensional atmospheric information with advanced deep learning offers a pathway toward extended lead times, multi-variable prediction, and more accurate characterization of severe weather. As multi-source observations and machine learning models continue to converge, such models are expected to play an increasingly important role in future severe weather forecasting and early warning systems.

## 4 Method

### 4.1 Data

The ERA5 reanalysis dataset [36], produced by the European Centre for Medium-Range Weather Forecasts (ECMWF), offers hourly global atmospheric data from January 1950 onward at a spatial resolution of approximately 31 km. To provide large-scale three-dimensional atmospheric information for FuXi-Nowcast training, we use a subset of ERA5 with a  $0.25^\circ$  spatial resolution and 1-hour temporal resolution. The data are linearly interpolated to  $0.01^\circ$  resolution and cropped to the region  $29.01^\circ\text{N}$  -  $36.68^\circ\text{N}$ ,  $114.67^\circ\text{E}$  -  $122.34^\circ\text{E}$  ( $768 \times 768$  grid points) to match the spatial domain of other observations (Figure 3).

As ERA5 data have an latency of about five days, they are unsuitable for real-time inference. During inference, we instead use FuXi-2.0 forecasts [34, 35], which provides continuous 1-hour forecasts at  $0.25^{\circ}$  resolution. We use 70 meteorological variables from FuXi-2.0 outputs, including five upper-air variables, such as geopotential (Z), temperature (T), u component of wind (U), v component of wind (V), and specific humidity (Q) across 13 pressure levels (50, 100, 150, 200, 250, 300, 400, 500, 600, 700, 850, 925, and 1000 hPa). Five surface variables are also included: 2-meter temperature (T2M), 10-meter u wind component (U10M), 10-meter v wind component (V10M), mean sea-level pressure (MSL), and total precipitation (TP). All variables are interpolated to 1-km resolution and cropped to the same target domain for consistency.

In addition to the three-dimensional atmospheric fields, multi-source ground observations are incorporated. Surface wind data, including 10-meter wind speed (WS10M) and wind gusts (GS), the maximum instantaneous wind speed over a short duration within an hour [37, 38], are collected from more than 1300 ground-based weather stations across Jiangsu Province (Figure 3). The WS10M data, originally available at 6-minute resolution, are averaged to hourly means, while GS values represent hourly maxima. Both datasets are spatially interpolated to the  $768 \times 768$  grid using inverse distance weighting [39, 40] to ensure spatial consistency with other inputs.

To provide direct precipitation information, radar composite reflectivity (CR) data are used with 1-km spatial and 6-minute temporal resolution, covering  $29.0^{\circ}\text{N} - 40.0^{\circ}\text{N}$ ,  $113.0^{\circ}\text{E} - 124.0^{\circ}\text{E}$  ( $1100 \times 1100\text{km}$ ). The 6-minute radar data are resampled to hourly resolution by extracting instantaneous values at each hour and cropped to the target domain.

The HRCLDAS dataset [41] integrates ground station observations, satellite data, and NWP model outputs, providing high-quality atmospheric analyses for model input and target. HRCLAS provides hourly meteorological fields at 1-km spatial resolution, covering China and adjacent regions ( $15^{\circ}\text{N} - 55^{\circ}\text{N}$ ,  $70^{\circ}\text{E} - 140^{\circ}\text{E}$ ). For this study, HRCLDAS data from April to September during 2019-2023 are used within the target domain. Five variables, such as 2-meter specific humidity (Q2M), total precipitation (TP), 10-meter u wind component (U10M), 10-meter v wind component (V10M), and 2-meter temperature (T2M) serve as the reference dataset for model training and evaluation.

Finally, a static land-sea mask from ERA5-Land [42] is included to distinguish surface types, enabling the model to capture systematic differences in the evolution of precipitation and wind fields over land and ocean.

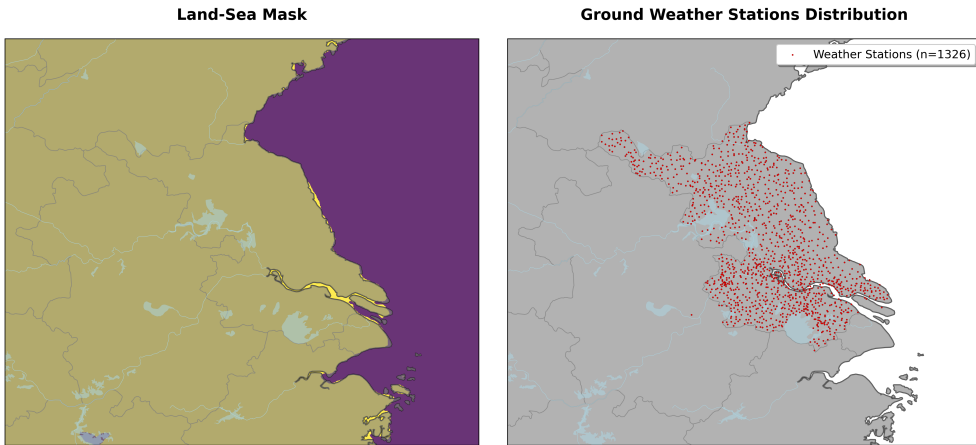


**Fig. 3** Spatial distribution of ground-based weather stations across Jiangsu Province. The station network consists of fixed station locations, with occasional data gaps at some stations during certain time periods.

FuXi-Nowcast is trained on data from April to September in each year from 2019 to 2023, and independently evaluated on the same period in 2024, supplemented by some cases in 2025. To prioritize high-impact weather events, a data filtering procedure is applied during training. Given the importance of severe convection in nowcasting, clear-sky and fair-weather samples are removed through a extreme-event filtering criterion: a sample is retained only if it contains more than 10 grid points with 1-hour accumulated precipitation exceeding 1 mm, or more than 10 grid points with wind gusts exceeding 10.8 m/s. This strategy effectively enriches the training dataset with high-impact weather cases while maintaining sufficient sample diversity. No filtering is applied to the testing dataset to ensure it represents all weather conditions.

**Table 1** A summary of multi-source meteorological datasets used by FuXi-Nowcast, including their original and target resolutions, variable specifications, and temporal coverage. The "Role" column clarifies whether each variable serves as both an input and an output, or is solely utilized as an input by our model.

Data Source	Role	Raw Resolution	Processed Resolution	Variables	Steps
FuXi Forecasts	I	721×1440 (0.25°)	768×768 (0.01°)	65 upper-air variables (Z, T, U, V, Q) 5 surface variables (T2M, U10M, V10M, MSL, TP)	3
Weather Stations	I & O	— (0°)	768×768 (0.01°)	WS10M, GS	3
Radar Reflectivity	I & O	1100×1100 (0.01°)	768×768 (0.01°)	CR	3
HRCLDAS	I & O	4500×7000 (0.01°)	768×768 (0.01°)	Q2M, TP, U10M, V10M, T2M	3
Land-Sea Mask	I	721×1440 (0.25°)	768×768 (0.01°)	Mask	1

## 4.2 CMA-MESO 3-km model

The outputs from the China Meteorological Administration Regional High-Resolution Numerical Weather Prediction System (CMA-MESO) are used in this study. Specifically, the 3-km resolution configuration (CMA-MESO 3-km) serve as the baseline NWP model for comparison with FuXi-Nowcast. This operational system, driven by initial and boundary conditions from the global CMA-GFS model, provides forecasts covers China and its surrounding regions [43]. For evaluation, we use CMA-MESO 3-km outputs of TP and diagnosed CR. The GS variable is estimated from WS10M. All 3-km CMA-MESO forecasts are interpolated to a 1-km grid over the target domain.

## 4.3 FuXi-Nowcast model

To address key challenges in nowcasting, including convection initiation and evolution, intensity decay, and multi-hazard prediction, we propose FuXi-Nowcast, a machine learning-based nowcasting model. Its key innovations include integrating large-scale three-dimensional atmospheric fields with high-resolution local meteorological observations within a unified framework to capture moisture and dynamic conditions that trigger convection, a convective feature enhancement module, a hybrid loss function for multi-variable forecasting, and multi-task learning for TP, enabling accurate forecasts up to 12 hours ahead.

The overall architecture of FuXi-Nowcast is shown in Figure 4. The model generates predictions in an autoregressive manner. The model input is a five-dimensional tensor of shape  $B \times T \times C \times H \times W$ , where  $B$  is the batch size,  $T$  is the number of preceding time steps ( $T=3$  for  $t-2$ ,  $t-1$ , and  $t$ ),  $C$  is the total number of input variables ( $C=78$ ), and  $H$  and  $W$  are the latitude (768) and longitude (768) grid points. The 78 variables combine 8 high-resolution local meteorological variables from HRCLDAS,

radar, and ground stations with 70 large-scale three-dimensional atmospheric variables from FuXi-2.0 (Table 1). During training, these three-dimensional fields are derived from ERA5 reanalysis, while during inference they are provided by FuXi-2.0.

The input tensor first passes through a convective signal enhancement module that selectively amplifies significant patterns via threshold-based pooling, enhancing convective relevant features while preserving spatial structure. The enhanced tensor is then processed by a embedding module, producing a feature map of shape  $B \times (T \times C) \times H \times W$ . Constant variables, including the land-sea mask and elevation data, are also encoded via a separate embedding module at this stage. Similarly, temporal features, such as forecasting step, hour of day, and day of year, is incorporated through an embedding module to provide temporal information.

In the feature extraction stage, the latent feature map is processed by 24 repeated Swin Transformer blocks, which capture complex spatiotemporal dependencies through global window attention and shifted-window mechanisms. In the upsampling and prediction stage, the decoder progressively restores the spatial resolution using adaptive transposed convolution modules, expanding the feature map from  $B \times 1024 \times H/12 \times W/12$  to the original  $768 \times 768$  grid. The decoder consists of two branches: a primary forecasting branch that outputs a tensor of shape  $B \times 1 \times 8 \times 768 \times 768$  for eight variables, and an auxiliary precipitation classification branch that outputs a tensor of shape  $B \times 1 \times 11 \times 768 \times 768$ , corresponding to 11 precipitation type categories. The predicted field is then appended to the historical sequence and concatenated with the 70 atmospheric variables from FuXi-2.0, enabling autoregressive forecasting up to 12 hours.

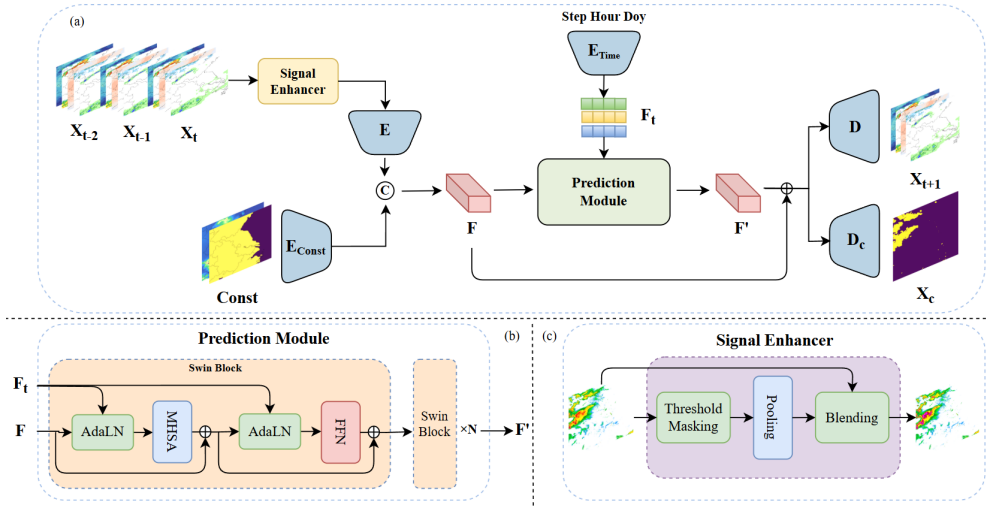


**Fig. 4** Schematic of the FuXi-Nowcast model. (a) Overall architecture of FuXi-Nowcast, which integrates large-scale atmospheric fields, high-resolution observations, and temporal embeddings as inputs. (b) Structure of the prediction module. (c) Design of the convective signal enhancement module.

#### 4.4 FuXi-Nowcast model training

As shown in Figure 5, the target variables exhibit distinct statistical characteristics. The T2M, U10M, and V10M variables show nearly symmetric distributions, whereas TP and CR demonstrate highly skewed, long-tailed distributions. Their probability density functions are dominated by numerous zero or near-zero values, with a small fraction of extreme events significantly extending the value range.

To accommodate these diverse distributions and effectively train our multi-task, multi-variable forecasting model, we constructed a hybrid loss function  $L_{\text{total}}$  that combines multiple components, each tailored to specific target variables.

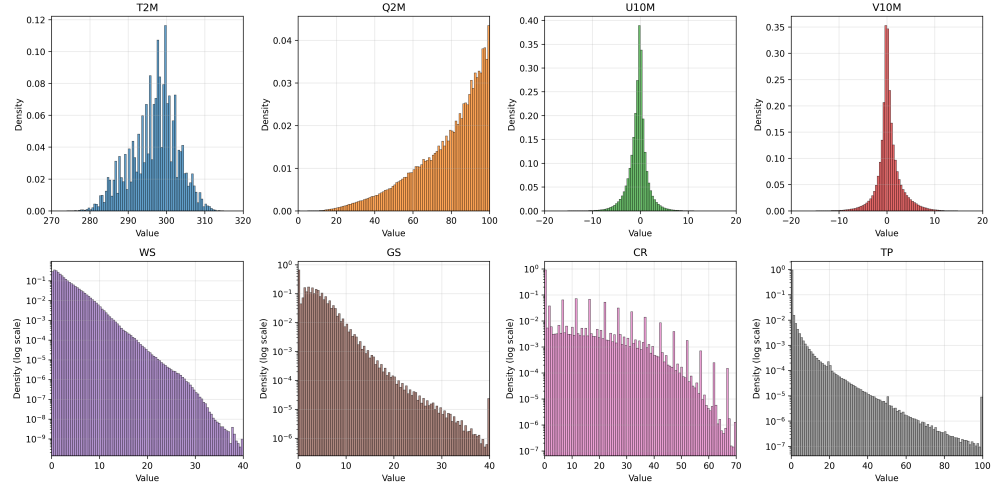


**Fig. 5** Statistical distributions of key forecast variables in the entire dataset. Columns 1 to 4 in the top row are 2-meter temperature (T2M), 2-meter specific humidity (Q2M), total precipitation (TP), 10-meter u wind component (U10M), 10-meter v wind component (V10M), and columns 1 to 4 in the bottom row are wind speed (WS), wind gusts (GS), composite reflectivity (CR), and total precipitation (TP). The y-axis shows probability density (top row) and log probability density (bottom row).

This formulation jointly optimizes regression accuracy, perceptual fidelity, and classification performance across different meteorological variables:

$$L_{\text{total}} = \lambda_{\text{cl1}} L_{\text{cl1}} + \lambda_{\text{bl1}} L_{\text{bl1}} + \lambda_{\text{lpips}} L_{\text{lpips}} + \lambda_{\text{SSIM}} L_{\text{SSIM}} + \lambda_{\text{focal}} L_{\text{focal}} + \lambda_{\text{dice}} L_{\text{dice}} \quad (1)$$

where  $L_{\text{cl1}}$  is the Charbonnier loss for regression,  $L_{\text{bl1}}$  is the Balanced L1 loss for handling extreme precipitation values,  $L_{\text{lpips}}$  is the LPIPS loss for perceptual similarity,  $L_{\text{SSIM}}$  is the SSIM loss for structural similarity,  $L_{\text{focal}}$  is the Focal loss for addressing class imbalance in precipitation classification, and  $L_{\text{dice}}$  is the Dice loss for spatial overlap optimization. The corresponding weights are set as  $\lambda_{\text{cl1}} = 1.0$ ,  $\lambda_{\text{bl1}} = 1.0$ ,  $\lambda_{\text{lpips}} = 0.1$ ,  $\lambda_{\text{SSIM}} = 0.1$ ,  $\lambda_{\text{focal}} = 1.0$ , and  $\lambda_{\text{dice}} = 0.1$ . This formulation jointly

optimizes regression accuracy, perceptual fidelity, and classification performance across different meteorological variables. The detailed formulations of each loss component are described as follows.

The Charbonnier loss [44]  $L_{cl1}$  is applied to all eight output variables. It measures the pixel-wise difference between the model's predictions and the ground truth. Its formula is defined as:

$$L_{cl1} = \sqrt{(\hat{\mathbf{X}} - \mathbf{X})^2 + \epsilon^2} \quad (2)$$

where  $\mathbf{X}$  is the ground truth and  $\hat{\mathbf{X}}$  is the predicted value.  $\epsilon$  is a small constant for numerical stability, which is set to 1e-6. The Charbonnier loss is a mix between L1 and L2 loss. When the prediction error is much larger than the small constant  $\epsilon$ , its property is similar to L1 loss, making it robust and insensitive to outliers in the data. Conversely, when the error approaches zero, its gradient behavior is more like L2 loss.

To address the issue of sparse samples for extreme values in the meteorological variable TP, we introduce the Balanced L1 Loss  $L_{bl1}$  [45, 46]. This loss function assigns higher loss weights to rare, high-intensity samples by calculating the sample frequency across different numerical intervals, thereby compelling the model to focus more on predicting these critical events during training. Its formula is defined as:

$$L_{bl1} = \sum_{i=1}^N w(\mathbf{X}_i) \cdot |\mathbf{X}_i - \hat{\mathbf{X}}_i| \quad (3)$$

where  $w(\mathbf{X}_i)$  is a weight determined by the numerical interval to which the ground truth  $\mathbf{X}_i$  belongs. In our implementation, we first partition the variable's value range into multiple bins based on predefined thresholds. For the TP variable, these thresholds are set to (0.1, 0.77, 1.86, 3.61, 6.43, 10.99, 18.33, 30.16, 49.24, 80, 100), creating 11 bins that are more uniformly distributed in the logarithmic domain, which more effectively delineates precipitation events of different magnitudes. This loss component is applied only to the TP variable.

To mitigate the blurring effect in deep learning-based forecasts and to ensure the generated fields are visually more realistic, we also introduce the Learned Perceptual Image Patch Similarity (LPIPS) loss  $L_{lpips}$ . The LPIPS loss compares the high-level feature differences between the predicted and ground truth images using a pre-trained deep network, thereby ensuring their perceptual similarity. In this study, we utilize a pre-trained VGG network for this purpose. The loss is formulated as:

$$L_{lpips} = \sum_l \frac{1}{H_l W_l} \sum_{h,w} w_l \cdot \|f_l^w(\mathbf{X}) - f_l^w(\hat{\mathbf{X}})\|_2^2 \quad (4)$$

where  $f_l^w(\mathbf{X})$  and  $f_l^w(\hat{\mathbf{X}})$  represent the feature vectors of the ground truth and predicted images at spatial location  $(h, w)$ , extracted from layer  $l$  of the network.  $H_l$  and  $W_l$  denote the height and width of the feature map at layer  $l$ , respectively. Therefore, the term  $\frac{1}{H_l W_l}$  serves to average the feature differences across the spatial dimensions, normalizing the loss contribution from feature maps at different scales. The term  $w_l$  is a learnable weight used to adjust the importance of different feature levels. This loss component is also applied to the WS, GS, CR, and TP variables.

Simultaneously, to further enhance the realism of the forecasts from an image structure perspective, we introduce the Structural Similarity Index Measure (SSIM) loss  $L_{\text{SSIM}}$ . Its formula is defined as:

$$L_{\text{SSIM}} = 1 - \frac{(2\mu_X\mu_{\hat{X}} + c_1)(2\sigma_{X\hat{X}} + c_2)}{(\mu_X^2 + \mu_{\hat{X}}^2 + c_1)(\sigma_X^2 + \sigma_{\hat{X}}^2 + c_2)} \quad (5)$$

where  $\mu$  and  $\sigma^2$  represent the mean and variance of the images, respectively,  $\sigma_{X\hat{X}}$  is the covariance of the two images, and  $c_1$  and  $c_2$  are small constants for maintaining stability, which are set to 1e-6 in our implementation. This loss component is also applied only to the WS, GS, CR, and TP variables.

For precipitation forecasting, tasks such as rain/no-rain classification suffer from a severe class imbalance problem, where easy samples like non-raining pixels significantly outnumber hard samples like raining pixels. To address this issue, we employ the Focal Loss  $L_{\text{focal}}$ , its formula is defined as:

$$L_{\text{focal}} = -\alpha_t(1 - p_t)^\gamma \log(p_t) \quad (6)$$

where  $p_t$  is the model's predicted probability for the true class. In our implementation,  $\gamma$  is set to 1.5. Additionally,  $\alpha_t$  is an optional weighting factor used to balance the importance of positive and negative samples, which is set to 0.25 in our implementation.

Finally, to further optimize the classification task from a spatial structure perspective, we introduce the Dice Loss  $L_{\text{dice}}$ . The core objective of this loss function is to maximize the spatial overlap between the predicted and ground truth precipitation areas at each class level. By minimizing the Dice loss, the model is encouraged to generate forecasts that are more spatially coherent and morphologically plausible. Its formula is:

$$L_{\text{dice}} = 1 - \frac{2|\mathbf{X} \cap \hat{\mathbf{X}}| + \epsilon}{|\mathbf{X}| + |\hat{\mathbf{X}}| + \epsilon} \quad (7)$$

In this formula,  $|\mathbf{X} \cap \hat{\mathbf{X}}|$  represents the number of pixels in the intersection of the predicted region  $\hat{\mathbf{X}}$  and the ground truth region  $\mathbf{X}$ , while  $|\mathbf{X}|$  and  $|\hat{\mathbf{X}}|$  represent the total number of pixels in each respective region.  $\epsilon$  is a small smoothing constant, which is set to 1.0 in our implementation. This parameter serves two main purposes: first, it effectively prevents computational instability caused by a zero denominator when both the prediction and the ground truth are empty; second, it also acts to smooth the loss function, which helps to stabilize gradients during the early stages of training or when dealing with small target areas. This loss component is also applied to the classification task for the TP variable.

The FuXi-Nowcast model is developed based on the Pytorch framework [47] and is trained in an end-to-end manner. We use the AdamW optimizer [48, 49], with the exponential decay rates for the first and second moment estimates set to  $\beta_1 = 0.9$  and  $\beta_2 = 0.95$ , respectively. We designed a learning rate schedule that employs a linear warm-up during the first 5% of the training steps, reaching a peak learning rate of

$2.5 \times 10^{-4}$ . Subsequently, the learning rate follows a cosine decay schedule, gradually decreasing to a minimum of  $5 \times 10^{-6}$  by the end of training.

## 4.5 Evaluation method

### 4.5.1 Critical Success Index

For the TP and GS variables, which require determining whether an event exceeds a specific threshold, we introduce the Critical Success Index (CSI). Its formula is as follows:

$$\text{CSI} = \frac{\text{TP}}{\text{TP} + \text{FP} + \text{FN}} \quad (8)$$

where TP represents the correctly forecasted events, FP refers to events that were predicted but did not occur, and FN indicates events that were observed but not forecasted. The CSI ranges from 0 to 1, with 1 representing a perfect forecast. A higher CSI value indicates better forecast performance, as it reflects the model's ability to identify events while minimizing both false alarms and missed events.

In our study, to evaluate the model's ability to forecast events of different intensities, we defined multiple thresholds for TP and GS. For the TP variable, the selected thresholds are 1, 5, 10, 20, 30, 40 and 50 mm/h; for the GS variable, the selected thresholds are 10.8, 13.9, and 17.2 m/s.

## Data Availability

The ERA5 reanalysis data are accessible through the Copernicus Climate Data Store at <https://cds.climate.copernicus.eu/>. ECMWF HRES forecasts can be retrieved from <https://apps.ecmwf.int/archive-catalogue/?type=fc&class=od&stream=oper&expver=1>. The data that support the findings of this study are available from Jiangsu Meteorological Observatory (JMO) of China Meteorological Administration (CMA). Restrictions apply to the availability of these data, which were used under license for this study.

## Acknowledgments

We appreciate the researchers at ECMWF for their invaluable contributions in collecting, archiving, disseminating, and maintaining the ERA5 reanalysis dataset.

## Competing interests

The authors declare no competing interests.

## References

- [1] Raymond, C., Matthews, T., Horton, R.M.: The emergence of heat and humidity too severe for human tolerance. *Science Advances* **6**(19), 1838 (2020) <https://doi.org/10.1126/sciadv.aaw1838>

- [2] Bojinski, S., Blaauboer, D., Calbet, X., De Coning, E., Debie, F., Montmerle, T., Nietosvaara, V., Norman, K., Bañón Peregrín, L., Schmid, F., *et al.*: Towards nowcasting in europe in 2030. *Meteorological applications* **30**(4), 2124 (2023)
- [3] Tripathy, K.P., Mukherjee, S., Mishra, A.K., Mann, M.E., Williams, A.P.: Climate change will accelerate the high-end risk of compound drought and heatwave events. *Proceedings of the National Academy of Sciences* **120**(28), 1–8 (2023)
- [4] Fowler, H.J., Blenkinsop, S., Green, A., Davies, P.A.: Precipitation extremes in 2023. *Nature Reviews Earth & Environment* **5**(4), 250–252 (2024)
- [5] Haslinger, K., Breinl, K., Pavlin, L., Pistotnik, G., Bertola, M., Olefs, M., Greilinger, M., Schöner, W., Blöschl, G.: Increasing hourly heavy rainfall in austria reflected in flood changes. *Nature* **639**(8055), 667–672 (2025)
- [6] Schmid, F., Wang, Y., Harou, A.: Nowcasting guidelines—a summary. *Bulletin* **68**, 2 (2019)
- [7] Chen, L., Cao, Y., Ma, L., Zhang, J.: A deep learning-based methodology for precipitation nowcasting with radar. *Earth and Space Science* **7**(2), 2019–000812 (2020)
- [8] Franch, G., Nerini, D., Pendasini, M., Coviello, L., Jurman, G., Furlanello, C.: Precipitation nowcasting with orographic enhanced stacked generalization: Improving deep learning predictions on extreme events. *Atmosphere* **11**(3), 267 (2020)
- [9] Sun, J., Xue, M., Wilson, J.W., Zawadzki, I., Ballard, S.P., Onvlee-Hooimeyer, J., Joe, P., Barker, D.M., Li, P.-W., Golding, B., *et al.*: Use of nwp for nowcasting convective precipitation: Recent progress and challenges. *Bulletin of the American Meteorological Society* **95**(3), 409–426 (2014)
- [10] Ravuri, S., Lenc, K., Willson, M., Kangin, D., Lam, R., Mirowski, P., Fitzsimons, M., Athanassiadou, M., Kashem, S., Madge, S., *et al.*: Skilful precipitation nowcasting using deep generative models of radar. *Nature* **597**(7878), 672–677 (2021)
- [11] Huang, L.X., Isaac, G.A., Sheng, G.: Integrating nwp forecasts and observation data to improve nowcasting accuracy. *Weather and forecasting* **27**(4), 938–953 (2012)
- [12] Sheridan, P.: Current gust forecasting techniques, developments and challenges. *Advances in Science and Research* **15**, 159–172 (2018)
- [13] Majumdar, S.J., Sun, J., Golding, B., Joe, P., Dudhia, J., Caumont, O., Chandra Gouda, K., Steinle, P., Vincendon, B., Wang, J., *et al.*: Multiscale forecasting of high-impact weather: Current status and future challenges. *Bulletin of the*

- [14] Hess, P., Boers, N.: Deep learning for improving numerical weather prediction of heavy rainfall. *Journal of Advances in Modeling Earth Systems* **14**(3), 2021–002765 (2022)
- [15] Roberts, R.D., Rutledge, S.: Nowcasting storm initiation and growth using goes-8 and wsr-88d data. *Weather and Forecasting* **18**(4), 562–584 (2003) [https://doi.org/10.1175/1520-0434\(2003\)018<0562:NSIAGU>2.0.CO;2](https://doi.org/10.1175/1520-0434(2003)018<0562:NSIAGU>2.0.CO;2)
- [16] Bai, L., Chen, G., Huang, L.: Convection initiation in monsoon coastal areas (south china). *Geophysical Research Letters* **47**(11), 2020–087035 (2020)
- [17] Dixon, M., Wiener, G.: Titan: Thunderstorm identification, tracking, analysis, and nowcasting—a radar-based methodology. *Journal of atmospheric and oceanic technology* **10**(6), 785–797 (1993)
- [18] Fleet, D., Weiss, Y.: Optical flow estimation. In: *Handbook of Mathematical Models in Computer Vision*, pp. 237–257. Springer, ??? (2006)
- [19] Han, L., Fu, S., Zhao, L., Zheng, Y., Wang, H., Lin, Y.: 3d convective storm identification, tracking, and forecasting—an enhanced titan algorithm. *Journal of Atmospheric and Oceanic Technology* **26**(4), 719–732 (2009)
- [20] Agrawal, S., Barrington, L., Bromberg, C., Burge, J., Gazen, C., Hickey, J.: Machine learning for precipitation nowcasting from radar images. *arXiv preprint arXiv:1912.12132* (2019)
- [21] Prudden, R., Adams, S., Kangin, D., Robinson, N., Ravuri, S., Mohamed, S., Arribas, A.: A review of radar-based nowcasting of precipitation and applicable machine learning techniques. *arXiv preprint arXiv:2005.04988* (2020)
- [22] Pulkkinen, S., Nerini, D., Pérez Hortal, A.A., Velasco-Forero, C., Seed, A., Germann, U., Foresti, L.: Pysteps: An open-source python library for probabilistic precipitation nowcasting (v1. 0). *Geoscientific Model Development* **12**(10), 4185–4219 (2019)
- [23] Wang, Y., Long, M., Wang, J., Gao, Z., Yu, P.S.: Predrnn: Recurrent neural networks for predictive learning using spatiotemporal lstms. *Advances in neural information processing systems* **30** (2017)
- [24] Espeholt, L., Agrawal, S., Sønderby, C., Kumar, M., Heek, J., Bromberg, C., Gazen, C., Carver, R., Andrychowicz, M., Hickey, J., *et al.*: Deep learning for twelve hour precipitation forecasts. *Nature communications* **13**(1), 1–10 (2022)
- [25] Andrychowicz, M., Espeholt, L., Li, D., Merchant, S., Merose, A., Zyda, F., Agrawal, S., Kalchbrenner, N.: Deep learning for day forecasts from sparse

observations. arXiv preprint arXiv:2306.06079 (2023)

[26] Casellas, E., Bech, J., Veciana, R., Pineda, N., Miró, J.R., Moré, J., Rigo, T., Sairouni, A.: Nowcasting the precipitation phase combining weather radar data, surface observations, and nwp model forecasts. *Quarterly Journal of the Royal Meteorological Society* **147**(739), 3135–3153 (2021)

[27] Sønderby, C.K., Espeholt, L., Heek, J., Dehghani, M., Oliver, A., Salimans, T., Agrawal, S., Hickey, J., Kalchbrenner, N.: Metnet: A neural weather model for precipitation forecasting. arXiv preprint arXiv:2003.12140 (2020)

[28] Zhang, Y., Long, M., Chen, K., Xing, L., Jin, R., Jordan, M.I., Wang, J.: Skilful nowcasting of extreme precipitation with nowcastnet. *Nature* **619**(7970), 526–532 (2023)

[29] Ibrahim, M., Alsheikh, A., Al-Hindawi, Q., Al-Dahidi, S., ElMoaqet, H.: Short-time wind speed forecast using artificial learning-based algorithms. *Computational intelligence and neuroscience* **2020**(1), 8439719 (2020)

[30] Chkeir, S., Anesiadou, A., Mascitelli, A., Biondi, R.: Nowcasting extreme rain and extreme wind speed with machine learning techniques applied to different input datasets. *Atmospheric Research* **282**, 106548 (2023)

[31] ECMWF: Atmospheric Model High Resolution 15-Day Forecast. <https://www.ecmwf.int/en/forecasts/datasets/set-i> Accessed 2025-06-30

[32] Shi, C., Jiang, L., Zhang, T., Xu, B., Han, S.: Status and Plans of CMA Land Data Assimilation System (CLDAS) Project. In: EGU General Assembly Conference Abstracts. EGU General Assembly Conference Abstracts, p. 5671 (2014)

[33] Han, S., Liu, B., Shi, C., Liu, Y., Qiu, M., Sun, S.: Evaluation of cldas and gldas datasets for near-surface air temperature over major land areas of china. *Sustainability* **12**(10) (2020) <https://doi.org/10.3390/su12104311>

[34] Zhong, X., Chen, L., Fan, X., Qian, W., Liu, J., Li, H.: FuXi-2.0: Advancing machine learning weather forecasting model for practical applications. Preprint at <https://arxiv.org/abs/2409.07188> (2024)

[35] Chen, L., Zhong, X., Zhang, F., Cheng, Y., Xu, Y., Qi, Y., Li, H.: Fuxi: A cascade machine learning forecasting system for 15-day global weather forecast. *npj climate and atmospheric science* **6**(1), 190 (2023)

[36] Hersbach, H., Bell, B., Berrisford, P., Hirahara, S., Horányi, A., Muñoz-Sabater, J., Nicolas, J., Peubey, C., Radu, R., Schepers, D., *et al.*: The era5 global reanalysis. *Quarterly journal of the royal meteorological society* **146**(730), 1999–2049 (2020)

- [37] Suomi, I., Vihma, T.: Wind gust measurement techniques—from traditional anemometry to new possibilities. *Sensors* **18**(4), 1300 (2018)
- [38] Chen, X., Ishihara, T.: A study of gust wind speed using a novel unsteady reynolds-averaged navier-stokes model. *Building and Environment* **267**, 112323 (2025)
- [39] You, J., Hubbard, K.G., Goddard, S.: Comparison of methods for spatially estimating station temperatures in a quality control system. *International Journal of Climatology* **28**(6), 777–788 (2008)
- [40] Zhao, W., Zhong, Y., Li, Q., Li, M., Liu, J., Tang, L.: Comparison and correction of idw based wind speed interpolation methods in urbanized shenzhen. *Frontiers of Earth Science* **16**(3), 798–808 (2022)
- [41] Han, S., Liu, B., Shi, C., Liu, Y., Qiu, M., Sun, S.: Evaluation of cldas and gldas datasets for near-surface air temperature over major land areas of china. *Sustainability* **12**(10), 4311 (2020)
- [42] Muñoz-Sabater, J., Dutra, E., Agustí-Panareda, A., Albergel, C., Arduini, G., Balsamo, G., Boussetta, S., Choulga, M., Harrigan, S., Hersbach, H., *et al.*: Era5-land: A state-of-the-art global reanalysis dataset for land applications. *Earth system science data* **13**(9), 4349–4383 (2021)
- [43] Liping, H., Liantang, D., Ruichun, W., Zhaorong, Z., Yuan, J., Zhifang, X., Lijuan, Z., Jin, Z., Lili, W., Fei, Y., *et al.*: Key technologies of cma-meso and application to operational forecast. *Journal of Applied Meteorological Science* **33**(6), 641–654 (2022)
- [44] Charbonnier, P., Blanc-Feraud, L., Aubert, G., Barlaud, M.: Two deterministic half-quadratic regularization algorithms for computed imaging. In: *Proceedings of 1st International Conference on Image Processing*, vol. 2, pp. 168–172 (1994). IEEE
- [45] Pang, J., Chen, K., Shi, J., Feng, H., Ouyang, W., Lin, D.: Libra r-cnn: Towards balanced learning for object detection. In: *Proceedings of the IEEE/CVF Conference on Computer Vision and Pattern Recognition*, pp. 821–830 (2019)
- [46] Shi, X., Gao, Z., Lausen, L., Wang, H., Yeung, D.-Y., Wong, W.-k., Woo, W.-c.: Deep learning for precipitation nowcasting: A benchmark and a new model. *Advances in neural information processing systems* **30** (2017)
- [47] Paszke, A., Gross, S., Massa, F., Lerer, A., Bradbury, J., Chanan, G., Killeen, T., Lin, Z., Gimelshein, N., Antiga, L., *et al.*: Pytorch: An imperative style, high-performance deep learning library. *Advances in neural information processing systems* **32** (2019)

- [48] Kingma, D.P., Ba, J.: Adam: A method for stochastic optimization. arXiv preprint arXiv:1412.6980 (2014)
- [49] Loshchilov, I., Hutter, F.: Decoupled weight decay regularization. arXiv preprint arXiv:1711.05101 (2017)